Science Bulletin 63 (2018) 1576–1582

Contents lists available at ScienceDirect

Science Bulletin

journal homepage: www.elsevier.com/locate/scib

Article

Direct synthesis of high-quality perovskite nanocrystals on a flexible substrate and deterministic transfer

Yilun Wang [a,b,1], Xing Cheng [a,1], Kai Yuan [a], Yi Wan [a], Pan Li [a], Yuhao Deng [a], Haoran Yu [a], Xiaolong Xu [a], Yi Zeng [a], Wanjin Xu [a], Yanping Li [a], Renmin Ma [a,b], Kenji Watanabe [c], Takashi Taniguchi [c], Yu Ye [a,b,*], Lun Dai [a,b,*]

[a] State Key Laboratory for Artificial Microstructure & Mesoscopic Physics, School of Physics, Peking University, Beijing 100871, China
[b] Collaborative Innovation Center of Quantum Matter, Beijing 100871, China
[c] National Institute for Materials Science, 1-1 Namiki, Tsukuba 305-0044, Japan

ARTICLE INFO

Article history:
Received 27 August 2018
Received in revised form 6 November 2018
Accepted 12 November 2018
Available online 24 November 2018

Keywords:
Deterministic transfer
$CsPbI_3$ nanocrystals
PDMS substrate
CVD

ABSTRACT

Solid-state perovskite nanocrystals are promising coherent light sources, as there is optical feedback within the crystal structure. In order to utilize the high performance of perovskites for on-chip applications, or observe new physical phenomena, these crystals must be integrated with pre-fabricated electronic or photonic structures. However, the material's fragility has made the deterministic transfer a great challenge thus far. Here, we report the first deterministic transfer of perovskite nanocrystals with sub-micron accuracy. Cesium lead halide ($CsPbI_3$) nanocrystals were directly synthesized on flexible polydimethylsiloxane (PDMS) stamps via chemical vapor deposition (CVD) and subsequently transferred onto arbitrary substrates/structures. We demonstrated the transfer of a $CsPbI_3$ crystalline nanoplate (NP) onto an 8 μm fiber core and achieved single-mode whispering gallery mode lasing. Our method can be extended to a variety of other arbitrary substrates (e.g., electrodes, photonic structures, micromechanical systems), laying the foundations for previously unattainable opportunities in perovskites-based devices.

1. Introduction

Solid-state lead halide perovskites exhibit excellent optical properties, due to its low defect density [1,2], high absorption efficiency [3,4], long charge carrier diffusion length [5–7], tunable band gap [8–10], etc. As a light source, the low threshold lasing of a $CH_3NH_3PbI_3$ nanowire (NW) was demonstrated at a carrier density as low as 10^{16} cm^{-3}, which is two orders of magnitude lower than those of conventional semiconductor NWs [11]. Recently, optically pumped continuous-wave lasing was realized in $CH_3NH_3PbI_3$ distributed feedback lasers, a key step towards an electrically pumped laser diode [12]. However, the aforementioned organic-inorganic based perovskites lacked chemical stability, leading to the synthesis of all-inorganic cesium lead halide perovskites ($CsPbX_3$, X = Cl, Br, or I). The chemical stability has enabled practical device applications as well as the study of fundamental physical properties [13–16]. Among the synthesis methods of lead halide perovskites, chemical vapor deposition (CVD) has become preferred over solution-based growth [13,17–19] in the production of high quality $CsPbX_3$ nanocrystals with a low surface recombination rate, low defect density, and well-defined morphology [20]. The advantages of CVD grown $CsPbX_3$ nanoplates (NPs) are apparent, when optical pumping of NPs resulted in built-in whispering gallery mode (WGM) lasers with low thresholds and high quality factors [21]. However, more complex fabrication or devices built on $CsPbX_3$ have been challenging, as it typically requires the perovskite on a goal substrate. The most common CVD growth of $CsPbX_3$ is on mica (as the perovskite can grow epitaxially on mica) [22], but the layered nature of mica makes assembling the $CsPbX_3$ into electronic/photonic devices unfeasible.

Inspired by other nanomaterials that can be successfully dry-transferred via a viscoelastic polydimethylsiloxane (PDMS) stamp [23,24], we report the first direct synthesis of $CsPbI_3$ nanocrystals on PDMS. In the CVD of $CsPbI_3$ on PDMS, we discovered how molten Pb nanoparticles on the PDMS surface served as catalysts for the growth of the $CsPbI_3$ nanocrystals. By changing the PDMS's temperature during deposition (i.e., changing the distance from the perovskite precursors), we were able to tune the $CsPbI_3$

* Corresponding authors.
E-mail addresses: ye_yu@pku.edu.cn (Y. Ye), lundai@pku.edu.cn (L. Dai).
[1] These authors contributed equally to this work.

https://doi.org/10.1016/j.scib.2018.11.014
2095-9273/

nanocrystal morphology from NP to NW. Furthermore, the flexible PDMS substrate directly served as the stamp for transferring specific $CsPbI_3$ nanocrystals onto the goal substrates. Using this deterministic dry transfer method, we transferred a $CsPbI_3$ NP with sub-micron spatial resolution onto the core of an optical fiber and observed single-mode lasing from the NP via optical pumping from the fiber's other end. The advances of the described synthesis and transfer methods facilitate the integration of perovskite nanocrystals with complex designer photonic structures, opening new routes for unexplored applications in communication, high-sensitivity sensors, high-resolution imaging, and others.

2. Experimental

2.1. Synthesis of $CsPbI_3$ NP on PDMS

The $CsPbI_3$ NPs were synthesized via a CVD method. A quartz boat loaded with the precursor (mixed powder of PbI_2 and CsI with molar ratio of 1:1) and PDMS (GEL PAK, PF-17-X4) substrates were inserted into a quartz tube placed inside a tube furnace, with the precursor upstream. The quartz tube was pumped down to 40 mTorr (1 mTorr ≈ 0.133 Pa) and then aerated with high-purity Ar gas to atmospheric pressure. During the growth, the temperature at the precursor was 500 °C. The growth process was 15 min under 25 sccm (standard cubic centimeters per minute) flow of high-purity Ar. After the synthesis, the quartz tube was cooled down naturally.

2.2. Atomic force microscopy

Atomic force microscopy (AFM) measurements were carried out with Cypher S (Asylum Research) in ambient condition using tapping mode.

2.3. First-principles calculations

The first-principles calculations were based on density functional theory (DFT) and the generalized gradient approximation (GGA), using the Cambridge Sequential Total Energy Package (CASTEP). The slab models, containing eight atomic layers with 10 Å vacuum spaces separating the slabs, were built. The top two layers at both sides of the slab were allowed to relax by minimizing the quantum-mechanical force on each ion site to be less than 0.001 eV/Å. Other layers were fixed in the optimized bulk configuration.

2.4. Optical characterizations of the $CsPbI_3$ NPs

Emission spectra of the $CsPbI_3$ NPs were measured under the excitation of a 532 nm nanosecond pulsed laser (repetition rate of 1 kHz, pulse duration of ~4.5 ns). A 10× objective lens (N.A. = 0.25) was used to couple the pumping light into one end of a fiber and a 100× objective lens (N.A. = 0.75) was used to collect the emission light from the other end (covered by a $CsPbI_3$ NP) of the fiber. The diameter of the fiber core was 8 μm. An Andor spectrometer (Shamrock 500i) equipped with an air cooled CCD (DU920P) was used for spectrum measurement.

2.5. Numerical calculations

Optical mode simulation for the rectangular $CsPbI_3$ NP depicted in Fig. 1e was performed using COMSOL multiphysics with parameters of refractive indices of $CsPbI_3$ (n_g = 3.25) and air (n_{air} = 1).

3. Results and discussion

3.1. Synthesis and characterization of $CsPbI_3$ nanocrystals on PDMS

To synthesize high-quality and transferrable $CsPbI_3$ nanocrystals via CVD, we used PbI_2 and CsI (molar ratio of 1:1) as precursors [21], and flexible PDMS as the substrate (see Experimental section). We find that PDMS does not (qualitatively) decompose in the conditions of our CVD growth (precursor temperature of 500 °C, substrate temperature of 221 °C), as the PDMS with $CsPbI_3$ deposited retains high flexibility and transparency after CVD (Fig. 1a). Regularly shaped $CsPbI_3$ nanocrystals, including NPs, NWs, and nanobelts, were found on both faces of the PDMS substrate (Fig. 1b). In addition, we found that changing the PDMS temperature (via PDMS distance from precursor) changed the morphology distribution of the $CsPbI_3$ from predominantly NPs to NWs (Fig. S1 online), indicating that the deposition temperature can significantly affect the nanocrystal shapes. The synthesized NPs were regular rectangles with edge lengths of several to tens of micrometers, due to the cubic crystalline structure of $CsPbI_3$. Our dark-field optical images showed a nanoparticle attached on the edges of the NPs (Fig. 1c), indicated by the circle in the inset. In addition, based on the AFM measurements (see Experimental section) in Fig. 1d, the diameter of this nanoparticle roughly matched the thickness of the NPs (150–450 nm, Fig. S2 online). The perovskite surface was identified as nearly atomically smooth, with a surface roughness of 0.38 nm (Fig. S3 online). Using EDX, we found that this particle on the edge was predominately Pb (Fig. 1e) with trace Cs and I, whereas the perovskite itself had uniform levels of all three elements. Coupled with absence of these particles when $CsPbI_3$ NPs were epitaxially grown on mica, and the fact that SiO_2/Si substrates were not able to facilitate the surface growth of $CsPbI_3$ (Fig. S4 online), we concluded that the Pb particle played a crucial role in the nucleation and growth of $CsPbI_3$ on PDMS. The room-temperature PL spectrum of an individual NP (Fig. 1f), via 532 nm laser excitation, revealed a strong near-band-edge emission centered at ~705 nm (~1.76 eV). The absence of defect related peaks in the spectrum and uniformity of the PL fluorescence mapping across the synthesized $CsPbI_3$ crystals (inset of Fig. 1f) proved that the as-synthesized $CsPbI_3$ NPs were of high quality. The energy gap extracted from the absorption spectrum of the NP was 1.75 eV (Fig. 1f), in good agreement with the PL data and previous reports [25,26]. As the exciton binding energy of $CsPbI_3$ is ~25 meV [27,28], smaller than the room-temperature thermal kinetic energy, the exciton oscillation peak was not observed in our absorption spectrum.

3.2. The growth mechanism of $CsPbI_3$ nanocrystals

To understand the possible growth mechanism of $CsPbI_3$ nanocrystals on PDMS via a nanoparticle nucleation site, we conducted transmission electron microscope (TEM) characterization and first-principles calculations. In the literature, PDMS was widely used as the substrate for the synthesis of silver nanoparticles, due to its high adhesion [29], which results from its low surface tension (20.4 mN/m) (lower surface tension as temperature increases) [30,31]. At temperatures greater than 180 °C, the PbI_2 can decompose to Pb and I_2 [32], while CsI does not undergo thermal dissociation at growth temperatures of 500 °C [33]. The high adhesion of PDMS enabled the Pb nanoparticles to distribute on its surface prior to the growth of $CsPbI_3$, which was confirmed by the dark-field optical imaging and EDX mapping (Fig. S5 online). At the substrate temperature of 221 °C, the PDMS did not decompose (Fig. S6 online). Subsequently, the precursor (CsI and PbI_2) vapor dissolved into the liquid Pb nanoparticles until

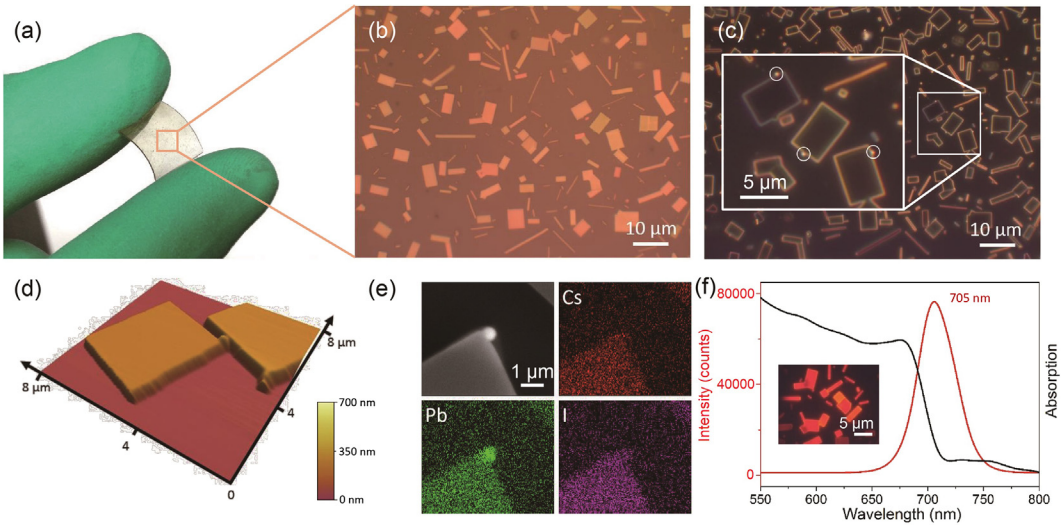

Fig. 1. (Color online) Characterizations of the synthesized $CsPbI_3$ nanocrystals. (a) Photograph of the PDMS substrate after the CVD process, showing its high flexibility and transparency after growth. (b) Bright-field optical image of the as-synthesized $CsPbI_3$ nanocrystals on the PDMS substrate. NPs, nanobelts and NWs distributed on the PDMS surface. (c) Dark-field optical image of the $CsPbI_3$ nanocrystals shown in Fig. 1b. The nanocrystals with different thicknesses or diameters exhibit different scattering colors. Significantly, almost every nanocrystal has a nanoparticle attached on the edge, which is difficult to discern from the bright-field image alone. Inset: the zoomed-in dark-field optical image, where the nanoparticles were marked with white circles. (d) AFM characterization of the $CsPbI_3$ NPs transferred onto a quartz substrate, which shows the NPs' smooth surface. (e) Energy dispersive X-ray spectroscopy (EDX) elemental mapping of Cs, Pb and I, at the NP edge. (f) Room-temperature photoluminescence (PL) and absorption spectra of a $CsPbI_3$ NP. Inset: mapping of the $CsPbI_3$ NPs PL.

saturation occurs. Thus, the Pb nanoparticles served as catalysts in the growth, which promoted the formation of plate-like $CsPbI_3$ seeds, due to the perovskite's cubic structure (Fig. 2a). The dissolution and crystal growth from the seed surface occurred simultaneously. The formation of the $CsPbI_3$ NPs and NWs could be explained by Gibbs-Curie-Wuff theorem, i.e., the normal growth rates of crystal faces are proportional to the corresponding surface free energies. The surface free energies of cubic $CsPbI_3$ (Fig. 2b) can be obtained via first-principles calculations based on DFT and the generalized gradient approximation (GGA), using the CASTEP (see Experimental section). The surface energy is defined by the follow function:

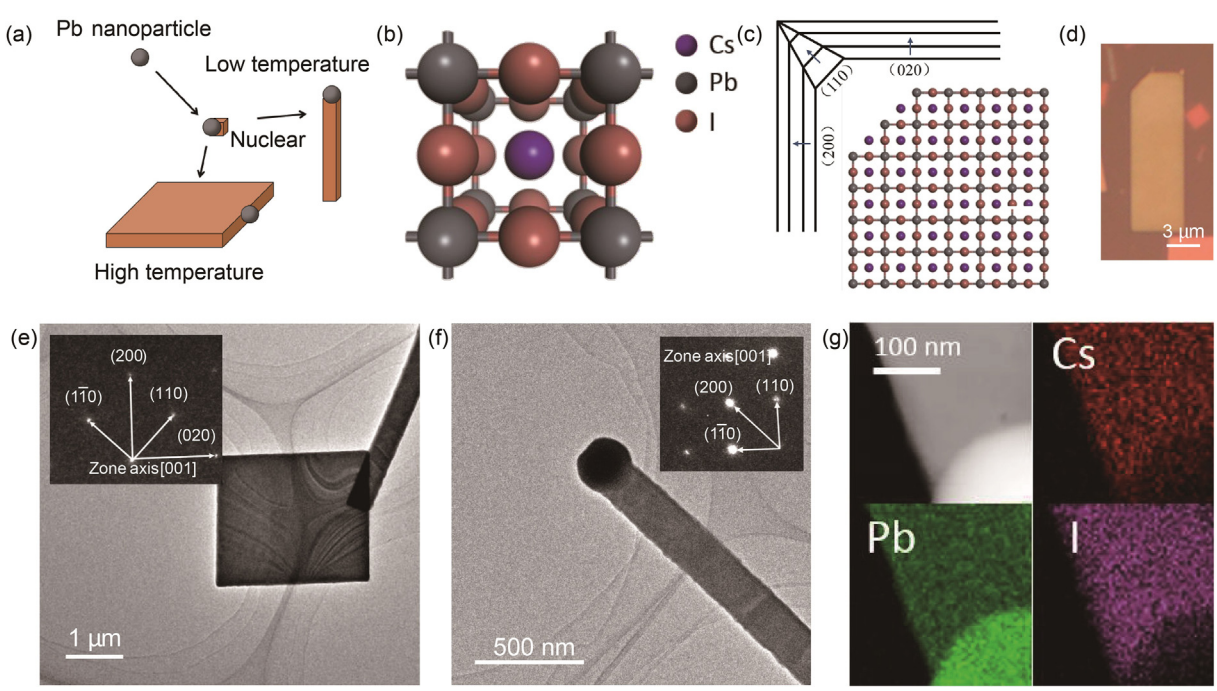

Fig. 2. (Color online) Growth mechanism and TEM characterizations of $CsPbI_3$ nanocrystals. (a) Schematic diagram of the nucleation and growth of the $CsPbI_3$ nanocrystals. The Pb nanoparticles served as catalysts for the growth of the nanocrystals. (b) Crystal structure of the cubic $CsPbI_3$. (c) Top-view ball-and-stick schematic illustration of a $CsPbI_3$ NP. The corresponding surfaces are labeled. According to the Gibbs-Curie-Wulff theorem, the corner is eventually filled due to the different growth rates of the different surfaces. (d) A representative NP with a truncated corner. By prolonging the growth time, the truncated corners are filled. (e) Low-magnification TEM image of a $CsPbI_3$ NP. Inset: SAED pattern of the $CsPbI_3$ NP. (f) Low-magnification TEM image of an as-grown $CsPbI_3$ NW. Inset: SAED pattern of the NW. At low substrate temperatures, the energy of the precursor vapor was insufficient to overcome the growth barrier of the (0 1 0) surface. (g) EDX mapping data that showed the elemental composition of the NW.

$$\varepsilon = \frac{E(n_{CsPbI_3}) - nE_{CsPbI_3}}{2A}, \quad (1)$$

where $E(n_{CsPbI_3})$ is the total energy of the surface slab of $CsPbI_3$, n is the number of units of $CsPbI_3$ in the surface slab, E_{CsPbI_3} is the bulk energy per $CsPbI_3$ unit, and A is the surface area. According to the theorem, the (0 0 1) surface with the lowest surface energy is the preferable lateral face of $CsPbI_3$ crystal because of its low growth rate (Fig. 2c). The (1 1 0) surface has higher surface energy than those of the (1 0 0) and (0 1 0) surface. At high substrate temperatures, the high energy of the precursor vapor can overcome the growth barriers of (1 0 0) and (0 1 0) surfaces, leading to the growth rate of (1 1 0) to be higher than those of (1 0 0) and (0 1 0), leading to the formation of a rectangular NP. The results of the calculations were verified experimentally, as we occasionally observed $CsPbI_3$ NPs with truncated corners (Fig. 2d), whose corners were filled with prolonged growth time. At low substrate temperatures, the energy of the precursor vapor was insufficient to overcome the growth barrier of (0 1 0) surface. The growth guided by the vapor-liquid-solid (VLS) mechanism resulted in a one-dimensional (1D) NW along the preferential [1 0 0] direction, which was also experimentally verified when the PDMS is placed at a lower temperature (Fig. S1 online). These results can be further confirmed using TEM, as the selected area electron diffraction (SAED) pattern of a typical rectangle $CsPbI_3$ NP showed that the top surfaces of the NPs belong to the (0 0 1) crystal lattice face, while the surfaces of the rectangular NPs were the (1 0 0) and (0 1 0) crystal faces (Fig. 2e). In the low temperature case, TEM showed that the $CsPbI_3$ NW grows along [1 0 0] direction (Fig. 2f), and the EDX mapping (Fig. 2g) confirmed the growth catalyst that terminates the NW is predominately Pb. Thus, the growth process is summarized as Pb particle adhesion on the PDMS surface and subsequent catalyzed growth into NPs or NWs based on the surface free energies (i.e., deposition temperature of the substrate).

3.3. Deterministic transfer of the $CsPbI_3$ NPs

Integration of $CsPbI_3$ nanocrystals through a site-controllable placement is necessary for the fabrication of more complex devices, potentially enabling both discovery of fundamental physical phenomena as well as new device exploration. However, the isolated transfer of CVD $CsPbI_3$ NPs was typically difficult, as the conventional mica substrate and the NPs transferred together due to the epitaxial growth mechanism and mica's layered structure (allowing it to be "peeled off") [22]. The direct CVD synthesis of $CsPbI_3$ nanocrystals on flexible PDMS can facilitate the dry transfer of specifically selected $CsPbI_3$ nanocrystals onto pre-designed structures. For example, placement of a $CsPbI_3$ NP nanolaser on the end of the fiber can enable a perfect fiber optic solution for high-sensitivity sensors and high-resolution imaging [34–36]. To demonstrate the feasibility and ease of this, we transferred a $CsPbI_3$ NP onto the core of a fiber and showed lasing from the NP. The transfer process was conducted under an optical microscope (Zeiss Axio Imager, A2m) with a long-working-distance optical objective and two three-axis manipulators (Newport 462 XYZ) (Figs. 3a and S7 online). First, as-grown $CsPbI_3$ on PDMS (also serving as the dry transfer stamp) with a specific $CsPbI_3$ NP was attached to a glass slide fixed to one three-axis manipulator with the NP facing down. A fiber core facing up was fixed on the other three-axis manipulator (Fig. 3b). As the PDMS stamp is transparent, the identification and alignment of the $CsPbI_3$ NP with the fiber's core were performed with sub-micrometer resolution under the microscope. Once the NP and the fiber's core were aligned (Fig. 3c), the stamp

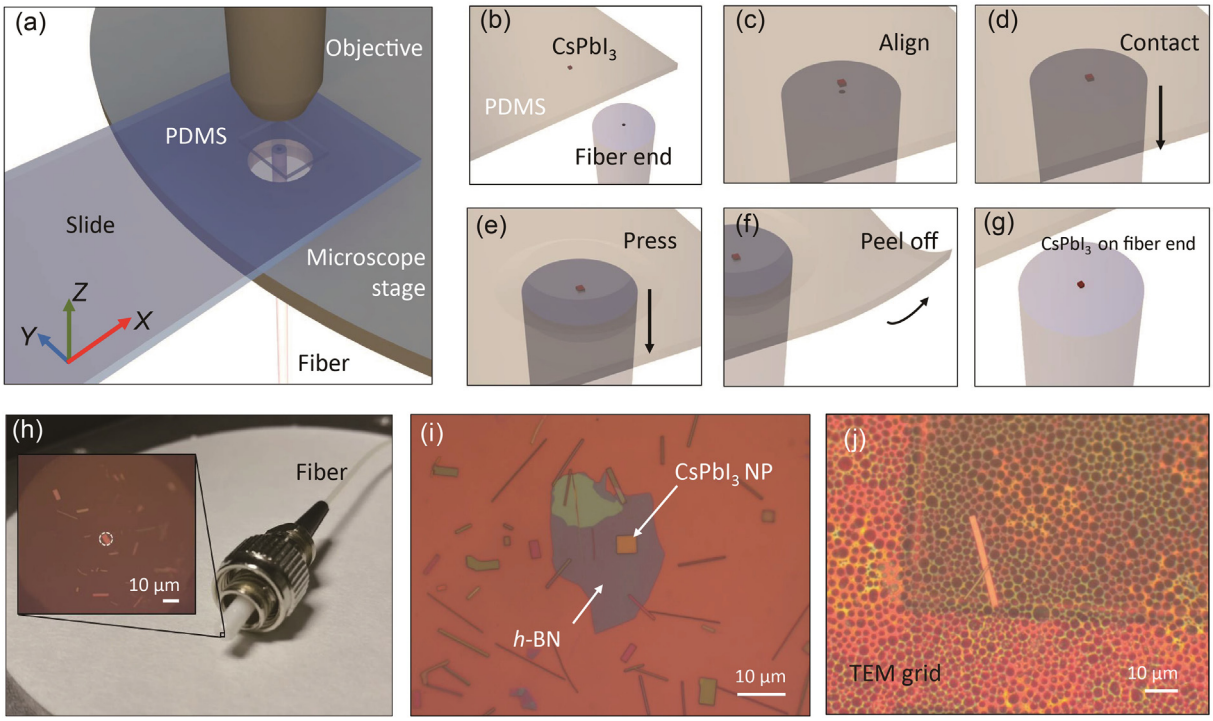

Fig. 3. (Color online) Deterministic transfer of $CsPbI_3$ nanocrystals. (a) Schematic diagram of the experimental setup employed for the all-dry transfer process. (b)–(g) The detailed procedure for transferring a $CsPbI_3$ NP onto the core of a fiber end. (b) An appropriate $CsPbI_3$ NP grown on PDMS was first selected using optical microscopy. A fiber with one end faced-up was fixed at one *XYZ* linear stage using a fiber holder. (c) The transparent PDMS substrate, adhered to window on a glass slide, was fixed on the other *XYZ* linear stage. The $CsPbI_3$ NP was aligned with sub-micron spatial resolution the cross section of the fiber's core using the two *XYZ* linear stages. (d) Once the alignment has been done, the $CsPbI_3$ NP was brought into contact with the fiber. (e) A pressing process was required in order to achieve contact. (f) The PDMS stamp was slowly peeled off. (g) The $CsPbI_3$ NP remained on the fiber end. (h) The photograph of a fiber end with a $CsPbI_3$ NP on the core of the fiber end. Inset: optical image of the fiber end with a $CsPbI_3$ NP on top. Dashed-line circle represents the fiber core. (i) Optical image of a $CsPbI_3$ NP on an *h*-BN flake. (j) Optical image of a TEM grid with transferred nanocrystals, including a $CsPbI_3$ NW and nanobelt.

was brought into contact with the fiber's core (Fig. 3d and e). Finally, the $CsPbI_3$ NP was left on the fiber's core by peeling off the stamp slowly (Fig. 3g and h). A detailed transfer process was provided in Fig. S8 (online). From our experiments, the transfer had nearly a 100% yield. The versatility of the transfer method was further demonstrated by transferring a $CsPbI_3$ NP onto an *h*-BN flake (Fig. 3i), allowing for future integration of perovskites with two-dimensional materials. Finally, the transfer method had been shown to be extremely gentle, as dry transfer of the $CsPbI_3$ nanocrystals on a fragile copper grid, which did not damage the crystals or grid (Fig. 3j).

3.4. $CsPbI_3$ NP lasing at a fiber end

Using the aforementioned dry transfer method, we deterministically placed a $CsPbI_3$ NP onto the core of an optical fiber in order to achieve fiber optic excitation of the NP lasing (Fig. 4a). To investigate the emission characteristics of the fiber laser, the $CsPbI_3$ NP on the fiber's core was optically pumped with a nanosecond-pulsed laser (4.5 ns pulse duration, 1.15 kHz repetition rate) coupled from the other side of the fiber (Fig. 4a) (see Experimental section). With a quasi-square shape and proper thickness, a $CsPbI_3$ NP simultaneously served as the laser's gain material and WGM resonant cavity, as given in the top inset of Fig. 4a (see Experimental section for more details) [21]. The excitation beam size was as large as fiber's core size (~8 μm) and covered the entire NP (the bottom inset of Fig. 4a). The emission spectra from the $CsPbI_3$ NP under different pump intensities were collected using a 100× objective lens with an N.A. of 0.75 (Fig. 4b). At low pump intensity (312.3 μJ/cm^2 per pulse), only a broad spontaneous emission peaked around 705.6 nm with an observed full width at half maximum (FWHM) of about 38.6 nm. As the pump intensity increased, a shoulder around 718.1 nm appeared which was comprised of the optical modes selectively amplified by the optical feedback in the NP WGM cavity. When the pump intensity surpassed 730 μJ/cm^2, the peak sharply increased in intensity. This left only one resonant peak with a much narrower FWHM (~0.77 nm), which was indicative of single-mode lasing behavior. Apparently, both the normalized spectra maps (inset of Fig. 4b) and the light-light (L-L) curve (Fig. 4c) showed a distinct kink with a super-linear increase in the emission output, with a lasing threshold extracted at ~730 μJ/cm^2. In addition, we clearly observed an abrupt spectrum narrowing above the lasing threshold (Fig. 4c). Using a rate equation analysis [37], the experimental data was best fit with a spontaneous emission factor (β) of 0.0062. Thus, we showed how a nanoscale single-mode $CsPbI_3$ NP laser could be integrated with fiber optics. This kind of single mode fiber laser with gain medium on top may potentially enable higher performance in fiber communication, high sensitivity sensors and high resolution imaging [34–36].

4. Conclusion

In summary, we successfully synthesized $CsPbI_3$ nanocrystals on PDMS substrates via CVD. We studied in detail the growth mechanism both theoretically and experimentally, ultimately

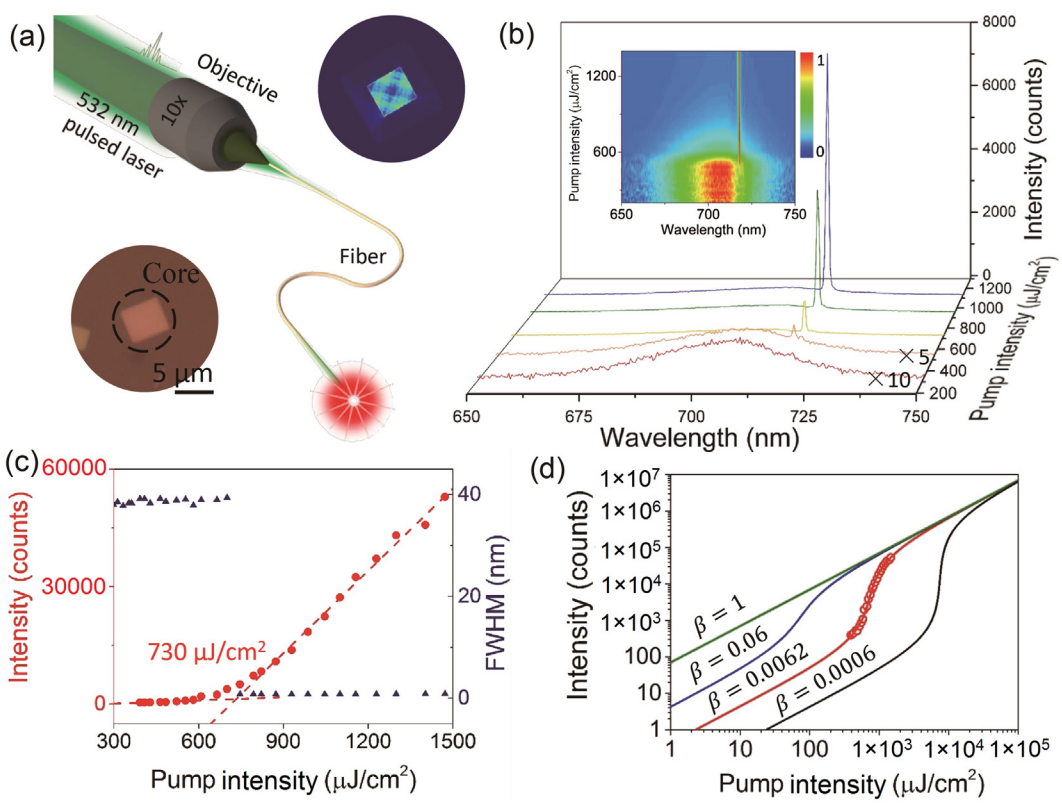

Fig. 4. (Color online) Lasing characteristics of $CsPbI_3$ NP on the core of a fiber end. (a) Schematic diagram of a $CsPbI_3$ NP on a fiber end pumped by a 532 nm pulsed-laser (duration of ~4.5 ns, repetition rate of 1.15 kHz), which was coupled in from the other end of the fiber. Top inset: absolute simulated electric field distribution of the transverse magnetic (TM) mode inside the NP (size: 5 μm × 4.5 μm). Clear WGM patterns were seen inside the cavity. Bottom inset: bright-field image of the $CsPbI_3$ NP. Dashed line circle represents the fiber's core. (b) Emission spectra from the $CsPbI_3$ NP on the fiber end under different excitation powers. Inset: the normalized spectral color map. As excitation power increased, the light emission changed from spontaneous emission to amplified spontaneous emission, and finally to lasing. (c) L-L curve plotted on a linear scale. Black lines represent linear fits to the experimental data, which yielded a threshold pump intensity of ~730 μJ/cm^2. The FWHM data of the emission peaks under different pump intensities were also provided. (d) Laser experimental data and rate equation analytical fits. The best fit to the experimental data gave with β of 0.0062. The calculated L-L curves with β of 0.0006, 0.06 and 1 were also presented for comparison.

proving that the molten Pb nanoparticles which adhered on the PDMS surface served as catalysts in the growth of the perovskite. In addition, the $CsPbI_3$ nanocrystal morphology (NP or NW) was controlled by changing the PDMS temperature. We also developed a deterministic dry transfer method of $CsPbI_3$ nanocrystals onto arbitrary substrates by using the flexible PDMS substrate as a stamp. As a demonstration, we transferred a $CsPbI_3$ crystalline NP on a fiber's core and realized single-mode lasing from the NP by optically pumping from the other end of the fiber. The advantages of the developed synthesis and transfer methods can facilitate the integration of perovskite nanocrystals with complex or custom-designed electronic/photonic structures, opening new routes for high-performance optoelectronics as well as discovery of new physical phenomena through integration with other nanomaterials.

Conflict of interest

The authors declare that they have no conflict of interests.

Acknowledgments

This work was supported by the National Natural Science Foundation of China (61875001, 61521004, 61874003, and 11474007), the National Key Research and Development Program of China (2018YFA0306900 and 2017YFA0206301), Beijing Natural Science Foundation (4182028), the National Basic Research Program of China (2013CB921901), and the "1000 Youth Talent Plan" Fund. Kenji Watanabe and Takashi Taniguchi acknowledge support from the Elemental Strategy Initiative conducted by the MEXT, Japan and the CREST (JPMJCR15F3), Yu Ye thanks Qing Zhang from Peking University for the helpful discussions.

Appendix A. Supplementary data

Supplementary data to this article can be found online at https://doi.org/10.1016/j.scib.2018.11.014.

References

[1] Shi D, Adinolfi V, Comin R, et al. Low trap-state density and long carrier diffusion in organolead trihalide perovskite single crystals. Science 2015;347:519–22.
[2] Ng A, Zhiwei R, Qian S, et al. Crystal engineering for low defect density and high efficiency hybrid chemical vapor deposition grown perovskite solar cells. ACS Appl Mater Interfaces 2016;8:32805–14.
[3] Hao F, Stoumpos CC, Cao DH, et al. Lead-free solid-state organic-inorganic halide perovskite solar cells. Nat Photon 2014;8:489–94.
[4] Jeon NJ, Noh JH, Kim YC, et al. Solvent engineering for high-performance inorganic-organic hybrid perovskite solar cells. Nat Mater 2014;13:897–903.
[5] Stranks SD, Eperon GE, Grancini G, et al. Electron-hole diffusion lengths exceeding 1 μm in an organometal trihalide perovskite absorber. Science 2013;342:341–4.
[6] Xing G, Mathews N, Sun S, et al. Long-range balanced electron-and hole-transport lengths in organic-inorganic $CH_3NH_3PbI_3$. Science 2013;342:344–7.
[7] Dong Q, Fang Y, Shao Y, et al. Solar cells. Electron-hole diffusion lengths >175 μm in solution-grown $CH_3NH_3PbI_3$ single crystals. Science 2015;347:967–70.
[8] Zhou H, Yuan S, Wang X, et al. Vapor growth and tunable lasing of band gap engineered cesium lead halide perovskite micro/nanorods with triangular cross section. ACS Nano 2017;11:1189–95.
[9] Wu K, Bera A, Ma C, et al. Temperature-dependent excitonic photoluminescence of hybrid organometal halide perovskite films. Phys Chem Chem Phys 2014;16:22476–81.
[10] Xing J, Liu XF, Zhang Q, et al. Vapor phase synthesis of organometal halide perovskite nanowires for tunable room-temperature nanolasers. Nano Lett 2015;15:4571–7.
[11] Zhu H, Fu Y, Meng F, et al. Lead halide perovskite nanowire lasers with low lasing thresholds and high quality factors. Nat Mater 2015;14:636–42.
[12] Jia Y, Kerner RA, Grede AJ, et al. Continuous-wave lasing in an organic–inorganic lead halide perovskite semiconductor. Nat Photon 2017;11:784.
[13] Eaton SW, Lai M, Gibson NA, et al. Lasing in robust cesium lead halide perovskite nanowires. Proc Natl Acad Sci USA 2016;113:1993–8.
[14] Ramasamy P, Lim DH, Kim B, et al. All-inorganic cesium lead halide perovskite nanocrystals for photodetector applications. Chem Commun 2016;52:2067–70.
[15] Chen CY, Lin HY, Chiang KM, et al. All-vacuum-deposited stoichiometrically balanced inorganic cesium lead halide perovskite solar cells with stabilized efficiency exceeding 11%. Adv Mater 2017;29:1605290.
[16] Dastidar S, Hawley CJ, Dillon AD, et al. Quantitative phase-change thermodynamics and metastability of perovskite-phase cesium lead iodide. J Phys Chem Lett 2017;8:1278–82.
[17] Sun S, Yuan D, Xu Y, et al. Ligand-mediated synthesis of shape-controlled cesium lead halide perovskite nanocrystals via reprecipitation process at room temperature. ACS Nano 2016;10:3648–57.
[18] Bekenstein Y, Koscher BA, Eaton SW, et al. Highly luminescent colloidal nanoplates of perovskite cesium lead halide and their oriented assemblies. J Am Chem Soc 2015;137:16008–11.
[19] Akkerman QA, Motti SG, Srimath Kandada AR, et al. Solution synthesis approach to colloidal cesium lead halide perovskite nanoplatelets with monolayer-level thickness control. J Am Chem Soc 2016;138:1010–6.
[20] Chen J, Morrow DJ, Fu Y, et al. Single-crystal thin films of cesium lead bromide perovskite epitaxially grown on metal oxide perovskite ($SrTiO_3$). J Am Chem Soc 2017;139:13525–32.
[21] Zhang Q, Su R, Liu X, et al. High-quality whispering-gallery-mode lasing from cesium lead halide perovskite nanoplatelets. Adv Funct Mater 2016;26:6238–45.
[22] Wang Y, Shi Y, Xin G, et al. Two-dimensional van der Waals epitaxy kinetics in a three-dimensional perovskite halide. Cryst Growth Des 2015;15:4741–9.
[23] Meitl MA, Zhu ZT, Kumar V, et al. Transfer printing by kinetic control of adhesion to an elastomeric stamp. Nat Mater 2006;5:33–8.
[24] Kim S, Wu J, Carlson A, et al. Microstructured elastomeric surfaces with reversible adhesion and examples of their use in deterministic assembly by transfer printing. Proc Natl Acad Sci USA 2010;107:17095–100.
[25] Swarnkar A, Marshall AR, Sanehira EM, et al. Quantum dot-induced phase stabilization of α-$CsPbI_3$ perovskite for high-efficiency photovoltaics. Science 2016;354:92–5.
[26] Palazon F, Almeida G, Akkerman QA, et al. Changing the dimensionality of cesium lead bromide nanocrystals by reversible postsynthesis transformations with amines. Chem Mater 2017;29:4167–71.
[27] Protesescu L, Yakunin S, Bodnarchuk MI, et al. Nanocrystals of cesium lead halide perovskites ($CsPbX_3$, X = Cl, Br, and I): novel optoelectronic materials showing bright emission with wide color gamut. Nano Lett 2015;15:3692–6.
[28] Saba M, Cadelano M, Marongiu D, et al. Correlated electron-hole plasma in organometal perovskites. Nat Commun 2014;5:5049.
[29] Kim JH, Park HW, Seo SW. In situ synthesis of silver nanoparticles on the surface of PDMS with high antibacterial activity and biosafety toward an implantable medical device. Nano Converg 2017;4:33.
[30] Sauer BB, Dee GT. Molecular weight and temperature dependence of polymer surface tension: comparison of experiment with theory. Macromolecules 1991;24:2124–6.
[31] Gohil SV, Suhail S, Rose J, et al. Materials for bone disorders. In: Susmita B, Amit B, editors. Cambridge: Academic Press; 2017. p. 349–503.
[32] Patnaik P. Handbook of inorganic chemicals. New York: McGraw-Hill; 2003.
[33] Kulikov IA, Malyshev ML. Radiation-chemical decomposition of CsI. Soviet Atomic Energy 1983;55:773–5.
[34] Liang Y, Jin L, Wang L, et al. Fiber-laser-based ultrasound sensor for photoacoustic imaging. Sci Rep 2017;7:40849.
[35] Iezzi VL, Loranger S, Kashyap R. High sensitivity distributed temperature fiber sensor using stimulated Brillouin scattering. Opt Express 2017;25:32591.
[36] Bai X, Liang Y, Sun H, et al. Sensitivity characteristics of broadband fiber-laser-based ultrasound sensors for photoacoustic microscopy. Opt Express 2017;25:17616–26.
[37] Wang S, Wang XY, Li B, et al. Unusual scaling laws for plasmonic nanolasers beyond the diffraction limit. Nat Commun 2017;8:1889.

Yilun Wang got his B.S. and Ph.D. degree from Peking University in 2013 and 2018, respectively. His research topic is novel nano-semiconductor photonics devices.

Lun Dai received her Ph.D. in Physics from Peking University in 1999. She is currently the director of the Institute of Condensed Matter and Material Physics, School of Physics, Peking University. She obtained the National Science Foundation for Outstanding Youth in 2011. Her research interest focuses on semiconductor materials and related device physics.

Yu Ye is an assistant professor in School of Physics at Peking University. He received his Ph.D. degree in condensed matter physics from Peking University in 2012. Prior to joining PKU in July 2016, Yu was working as a postdoctoral researcher at University of California, Berkeley. His group currently is interested in light-matter interactions and electrical transport properties in condensed matter physics, with an emphasis on novel physical phenomena emerging in atomically-thin materials, van der Waals heterostructures and surfaces/interfaces by nanoscale device designs, optical spectroscopy, electrical transport, and scanning photocurrent measurements.